ACS Catalysis

Research Article

pubs.acs.org/acscatalysis

First-Principles-Based Microkinetics Simulations of Synthesis Gas Conversion on a Stepped Rhodium Surface

Ivo A. W. Filot, Robin J. P. Broos, Jeaphianne P. M. van Rijn, Gerardus J. H. A. van Heugten, Rutger A. van Santen, and Emiel J. M. Hensen*

Laboratory of Inorganic Materials Chemistry, Schuit Institute of Catalysis, Department of Chemical Engineering and Chemistry, Eindhoven University of Technology, P.O. Box 513, 5600 MB Eindhoven, The Netherlands

Supporting Information

ABSTRACT: The kinetics of synthesis gas conversion on the stepped Rh(211) surface were investigated by computational methods. DFT calculations were performed to determine the reaction energetics for all elementary reaction steps relevant to the conversion of CO into methane, ethylene, ethane, formaldehyde, methanol, acetaldehyde, and ethanol. Microkinetics simulations were carried out on the basis of these first-principles data to predict the CO consumption rate and the product distribution as a function of temperature. The elementary reaction steps that control the CO consumption rate and the selectivity were analyzed in detail. Ethanol formation can only occur on the stepped surface, because the barrier for CO dissociation on Rh terraces is too high; step-edges are also required for the coupling reactions. The model predicts that formaldehyde is the dominant product at low temperature, ethanol at intermediate temperature, and methane at high temperature. The preference for ethanol over long hydrocarbon formation is due to the lower barrier for C(H) + CO coupling as compared with the barriers for CH_x + CH_y coupling reactions. The C(H)CO surface intermediate is hydrogenated to ethanol via a sequence of hydrogenation and dehydrogenation reactions. The simulations show that ethanol formation competes with methane formation at intermediate temperatures. The rate-controlling steps are CO removal as CO_2 to create empty sites for the dehydrogenation steps in the reaction sequence leading to ethanol, CH_xCH_yO hydrogenation for ethanol formation, and CH_2 and CH_3 hydrogenation for methane formation. CO dissociation does not control the overall reaction rate on Rh. The most important reaction steps that control the selectivity of ethanol over methane are CH_2 and CH_3 hydrogenation as well as $CHCH_3$ dehydrogenation.

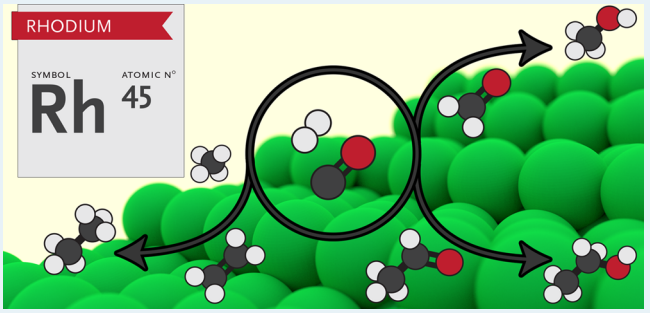

KEYWORDS: *rhodium, synthesis gas, ethanol, mechanism, DFT, microkinetics, selectivity*

1. INTRODUCTION

The expected decline in readily available fossil fuel resources motivates the search for alternative sources of fuels and chemicals. The Fischer−Tropsch reaction converts synthesis gas obtained from abundant and cheap natural gas by reforming or gasification into liquid transportation fuels. These gas-to-liquids processes are increasingly practiced at the industrial scale as an economically viable alternative to crude oil refining. The active phase in industrial Fischer−Tropsch catalysts typically comprises Fe or Co nanoparticles.[1−5] Ru is also active in the Fischer−Tropsch reaction, but it is too expensive for commercial production of fuels. Co, Fe, and Ru are suitable transition metals for Fischer−Tropsch synthesis of long-chain hydrocarbons, because they can dissociate CO at sufficiently high rates to maintain a high rate of chain growth.[6,7]

The decreased rate of CO dissociation on transition metals such as Ni, Cu, Rh, Pd, Ir, and Pt results in different products. For instance, the main product on Ni is methane. Transition metals such as Cu, Pd, Ir, and Pt do not dissociate CO, and accordingly, methanol is the main product.[8,9] On Rh, ethanol is one of the major reaction products besides methane.[8] Ethanol is an attractive intermediate for the production of valuable light olefins.[10] Many experimental works have focused on increasing the ethanol yield of Rh-based catalysts.[11−21] Rh catalysts also produce olefins (primarily ethylene) and other oxygenates (mainly methanol, acetaldehyde, and acetic acid). Although the formation of C_2-oxygenates is usually attributed to the intermediate CO dissociation activity,[8,22] mechanistic details about the reaction mechanism for Rh-based CO hydrogenation are lacking.

Quantum-chemical modeling based on density functional theory (DFT) can predict with reasonable accuracy the kinetic parameters for the elementary reaction steps that underlie the mechanism of heterogeneous reactions. The use of first-principles kinetic parameters in microkinetics simulations can provide detailed insight into the sensitive dependence of catalyst performance on the topology of the catalytic surface as

Received: July 4, 2015
Published: July 22, 2015

DOI: 10.1021/acscatal.5b01391
ACS Catal. 2015, 5, 5453−5467

well as the composition of the adsorbed layer under reaction conditions.[23−25] Due to the rapid advances in computing power, it has become feasible to carry out comprehensive studies of increasingly complex catalytic reactions such as the Fischer−Tropsch reaction.[26,27] In our recent work, we resolved important issues relevant to the Fischer−Tropsch reaction such as catalytic site requirements, the nature of chain propagation, and the influence of the reactivity of the transition metal.[27] The active reaction centers for the Fischer−Tropsch reaction are most likely step-edge sites on nanoparticle surfaces that display unique reactivity toward CO bond dissociation.

Pertinent issues concerning synthesis gas conversion by Rh catalysts relate to the optimum site for CO dissociation, the possible assistance of the CO dissociation step by H atoms, the nature of the surface coupling reactions that give rise to ethanol and ethylene and, from a practical point of view, how ethanol competes with formation of other products such as methane, higher hydrocarbons, and methanol. Theoretical studies about synthesis gas conversion by Rh have typically focused on too few elementary reaction steps to resolve these issues. Planar Rh(111) and stepped Rh(211) surfaces have typically been used as the surface models.[9,23,24,28−32] A detailed first-principles mechanistic study of CO conversion that clarifies these issues for Rh nanoparticle catalysts is lacking. Mei et al. carried out kinetic Monte Carlo simulations to understand the promoting effect of MnO_2 on Rh.[33] This work is hampered by the quality of the input because of the use of the less accurate UBI−QEP method to determine the activation energies.

The activation energy for CO dissociation on the Rh(111) terrace surface is very high (E_a > 250 kJ/mol).[9,23,28,30] Choi and Liu have shown that H-assisted CO dissociation involving the formyl (HCO) intermediate is more favorable than direct CO dissociation on close-packed surfaces.[9] We demonstrated that the barrier for CO dissociation on the stepped (211) surface is much lower than on the (111) and (100) terrace surfaces of Rh.[28] In line with these findings, Kapur and co-workers concluded that H-assisted CO dissociation via CHOH is the preferred reaction pathway on Rh(111), whereas the most favorable path on Rh(211) is direct CO dissociation.[22] DFT calculations combined with microkinetics simulations of the steam methane reforming reaction showed that CO formation via HCO competes with direct CO formation for Rh(211).[24,28] C−C coupling reactions on Rh surfaces have also been investigated by quantum-chemical modeling.[9,22,29,34] Choi and Liu concluded that CH_3 + CO coupling is the main reaction pathway to C_2-oxygenates on Rh(111).[9] Alternatively, Kapur et al. found that CH_2 + CO coupling is the most feasible route for C_2-oxygenate formation on Rh(211).[22] The ethanol decomposition reaction has also been studied in the past;[29,35−38] for instance, Zhang et al. reported that ethanol decomposition proceeds via CH_3CO dissociation on Rh(111) and Rh(211) surfaces. The lowest barrier was identified for the stepped surface.[29]

In the present study, we report results of quantum-chemical DFT investigations of the elementary reaction steps for CO conversion to methane, ethylene, formaldehyde, methanol, and ethanol on the stepped Rh(211) surface. The choice for the stepped surface is motivated by the low CO dissociation barrier on this surface as compared with terrace surfaces.[28] We chose the B_5 site of the stepped Rh(211) surface as a model for the different types of step-edge sites that may occur on nanoparticles. These step-edge sites will have different surface topologies. Our assumption is that the use of Rh(211) captures the most important aspects of stepped surfaces in comparison to close-packed surfaces. A large number of coupling reactions between CH_x species and CO were taken into account in this study. The O atoms originating from CO dissociation can be removed as water or carbon dioxide, or they can couple as O or OH to CH_x intermediates. On the basis of these first-principles kinetic data, we constructed a microkinetics model for the conversion of synthesis gas on the stepped surface. With this model, overall reaction rates, the product distribution, and kinetic parameters such as apparent activation energies and reaction orders were computed as a function of the temperature. A comparison with the Rh(111) surface was made on the basis of published DFT data. We performed a detailed analysis of the reaction network. To identify the steps that control the CO consumption rate and the product distribution, we employed the concepts of the degree of rate control (DRC) developed by Kozuch and Shaik[39,40] and the degree of selectivity control (DSC) introduced by Campbell.[41,42] We have expanded the DSC concept by correlating the DSC values of two different products in such way that competing dependencies in the reaction network can be identified. To the best of our knowledge, this is the first comprehensive first-principles-based microkinetics study of Rh-catalyzed synthesis gas conversion.

2. METHODS

All DFT calculations were performed using the plane-wave approach with the projector-augmented wave (PAW) method[43] implemented in the Vienna Ab Initio Simulation Package (VASP).[44,45] The Perdew−Burke−Ernzerhof (PBE) exchange correlation functional was used.[46] The kinetic energy cutoff for the plane-wave basis set was 400 eV, and a Brillouin zone sampling of 5 × 5 × 1 *k*-points was used. Partial occupancies were determined using a first order Methfessel−Paxton scheme with a smearing width of 0.2 eV. We modeled the Rh(211) termination of fcc Rh (Figure 1) with a theoretical Rh−Rh distance of 2.71 Å in a 3 × 2 supercell consisting of eight-layered slabs with periodic boundary conditions. All atoms were allowed to relax. In order to avoid spurious interactions between system images, a vacuum layer of at least 10 Å was added perpendicular to the surface between the adsorbed

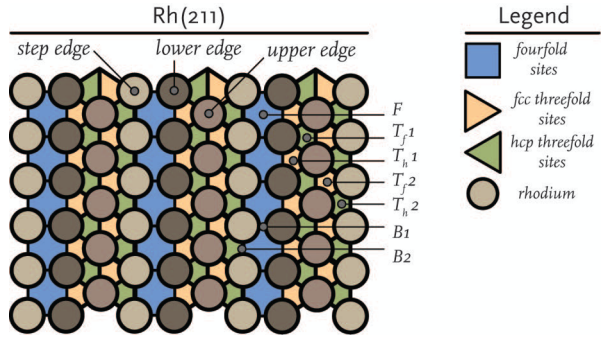

Figure 1. Schematic representation of the stepped Rh(211) surface. The coordination number (CN) of the surface atoms are CN = 7 for the step-edge, CN = 9 for the upper edge, and CN = 10 for the lower edge. The different shadings for the Rh atoms match the different coordination numbers of the surface metal atoms, where darker shadings represent higher coordination numbers. The adsorption sites for this surface include one 4-fold (F), two 3-fold fcc (T_f), two 3-fold hcp sites (T_h), and two bridge (B) sites.

DOI: 10.1021/acscatal.5b01391
ACS Catal. 2015, 5, 5453−5467

species. To confirm that the vacuum layer was large enough, we verified that the electron density approached zero at the border of the supercell. For the calculation of adsorption energies, gas-phase energies of molecules were performed by placing a molecule at the center of a large unit cell (typically 10 × 10 × 10 Å) using only the Γ-point for *k*-point sampling. Gaussian smearing with a width of 0.002 eV was used. Zero-point energy corrected reaction enthalpies based on these gas phase energies compared well with tabulated thermodynamic data within the accuracy of DFT.

To avoid dipole−dipole interactions between supercells, we placed the adsorbates on both sides of the slab and retained an inversion center for the dipole. Electronic convergence was set to 10^{-5} eV, and geometries were converged to 10^{-4} eV using a conjugate-gradient algorithm that employs trial and corrector steps to converge both the energy of the structure as well as the forces on the ions. To determine transition states, we employed the nudged elastic band (NEB) method developed by Jónsson et al.[47] All optimized transition geometries corresponded to a first-order saddle point on the potential energy surface, as verified by frequency analysis. The vibrational frequencies of local minima and transition states were computed using the finite displacement method. The Hessian matrix in this method was constructed using a finite displacement scheme with a step size of 0.02 Å. These frequencies were then used to determine the zero-point energy (ZPE) correction to the electronic energy. The computed Rh−Rh bulk distance of 2.71 Å and the cohesive energy of −5.91 eV/atom correspond well to experimental values of 2.69 Å and −5.75 eV/atom.[48]

The activation barriers and corresponding vibrational frequencies of the initial, transition, and final states were used to compute forward and backward rate constants for the elementary reaction steps relevant to synthesis gas conversion. For this purpose, the rate constant of each elementary surface reaction step was determined using the Eyring equation:

$$k = \frac{k_b T}{h}\frac{Q^{\ddagger}}{Q} e^{-E_a/k_b T} \tag{1}$$

where k is the rate constant in s^{-1}, k_b is the Boltzmann constant, T is the temperature in K, h is Planck's constant, $Q‡$ is the partition function of the transition-state complex, Q is the partition function of the complex in the preactivated (initial) state, and E_a is the electronic activation energy. The partition functions for the activated and preactivated complexes were taken as the products of the translational, rotational, and vibrational partition functions corresponding to the configurational degrees of freedom of the surface complexes.

To account for the entropy of the rotating methyl groups, the partition function of the classical expression for a hindered rotor (q_{HR}) was used. For a methyl group, the partition function becomes

$$q_{HR} = \frac{(2\pi)^{3/2} R}{h}\sqrt{3 k_b T m_H} \tag{2}$$

where R is the C−H bond length and m_H is the mass of a hydrogen atom.

For nonactivated molecular adsorption, it was assumed that the complex loses one translational degree of freedom with respect to the gas phase in the transition state. The changes in the rotational degrees of freedom were neglected. Accordingly, the following expression was employed for the rate of molecular adsorption:

$$k = \frac{PA}{\sqrt{2\pi m k_b T}} S \tag{3}$$

where P is the partial pressure of the adsorbate in the gas phase (in Pa), A is the surface area of the adsorption site (in m^2), m is the mass of the adsorbate (in kg), and S is the dimensionless sticking coefficient. The surface area A was set to the area of a 3-fold site, which is taken 3.1×10^{-20} m^2. The sticking coefficients were set to unity in the current simulations.

For desorption, it was assumed that the complex has three rotational degrees of freedom and two translational degrees of freedom in the activated state, while it has only vibrational degrees of freedom in the adsorbed state. Accordingly, the rate of desorption is given by ref 49

$$k = \frac{k_b T^3}{h^3}\frac{A(2\pi m k_b)}{\sigma \theta_{rot}} e^{-E_{des}/k_b T} \tag{4}$$

where σ is the (dimensionless) symmetry number, θ is the characteristic temperature for rotation (in K), and E_{des} is the desorption energy (in J/mol).

The approach for the microkinetics simulations was as follows. The surface was represented by a single adsorption site and all adsorbates occupy exactly one site. Differential equations for all surface reaction intermediates were constructed using the rate constants of the elementary steps. Given a system of N elementary reaction steps, $2N$ rate expressions (i.e., both forward and backward reactions) were obtained with the form:

$$r_j = k_j \prod_i c_i^{\upsilon_i^j} \tag{5}$$

where c_i is the concentration of species i in the elementary reaction step j on the surface (in mol species/mol catalytic sites), and ν_i is the stoichiometric coefficient of species i in elementary reaction step j. These rate expressions were used to derive an ordinary differential equation for each component on the surface with the form:

$$\frac{dc_i}{dt} = \sum_j \upsilon_{i,j} r_j \tag{6}$$

where c_i is the dimensionless concentration of species i on the surface, and $\nu_{i,j}$ the dimensionless stoichiometric coefficient of species i in elementary reaction step j.

The in-house-developed C++ program MKMCXX[50] was employed to determine the steady-state coverages by integrating this set of ordinary differential equations with respect to time using the backward differentiation formula method. The steady-state surface coverage values were used to compute the rates of the individual elementary reaction steps and the overall rate per surface atom.

3. RESULTS AND DISCUSSION

3.1. DFT Calculations. We performed DFT calculations for most of the elementary reaction steps relevant to the formation of hydrocarbons (methane, ethylene, and ethane) and oxygenates (formaldehyde, methanol, acetaldehyde, and ethanol). These reaction steps were grouped as follows: (i) direct and hydrogen-assisted CO dissociation reactions; (ii) C hydrogenation reactions to CH_x intermediates and CH_4; (iii) CO hydrogenation reactions to methanol; (iv) CH_x + OH_y, (v) CH_x + CH_y and (vi) CH_x + CO coupling reactions; (vii)

DOI: 10.1021/acscatal.5b01391
ACS Catal. 2015, 5, 5453−5467

CH_xCH_y and (viii) $CH_xCH_yOH_z$ hydrogenation reactions; and (ix) O removal reactions that involve formation of H_2O or CO_2. The values for the activation barriers are shown together with the reaction networks that convert CO and H_2 into C_1 products (methane, formaldehyde, methanol, and CO_2) in Figure 2 and into C_2 products (ethylene, ethane, acetaldehyde,

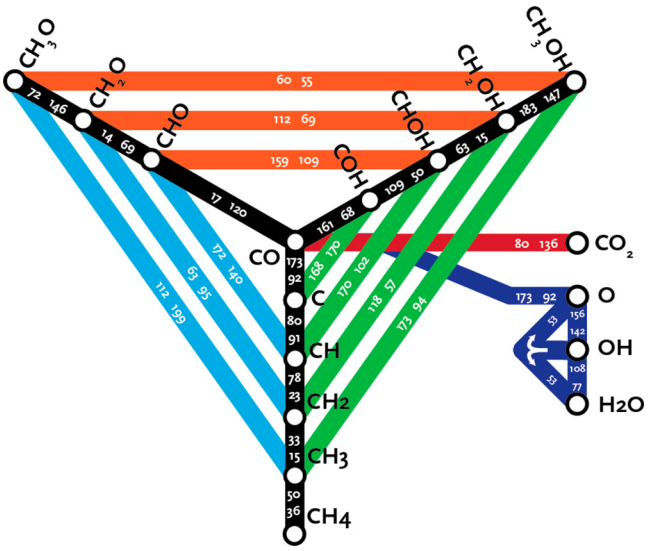

Figure 2. Forward and backward activation energies (kJ/mol) for the conversion of CO to CH_2O, CH_3OH, CH_4, CO_2, and H_2O. The first number going from one species to the next is the forward activation energy. For instance, the activation energy for CO dissociation is 173 kJ/mol; the activation energy for the backward reaction is 92 kJ/mol.

and ethanol) in Figure 3. The activation barriers are given with respect to the most stable adsorbed state for each intermediate. We corrected the barriers for the migration of fragments after dissociation by considering the energy difference of the geometry directly after dissociation and their most stable adsorption positions at infinite distance. We will first discuss the different adsorption sites and geometries of the intermediates. Then, we briefly discuss the individual elementary reaction steps and highlight the main trends in activation energies and transition-state structures. All these adsorption sites and elementary reaction steps along with the corresponding forward and backward activation energies are tabulated in the Supporting Information.

3.1.1. Adsorption Sites. Figure 1 shows the 2-, 3-, and 4-fold bridge and top adsorption sites on the Rh(211) surface. Table S1 lists the most stable adsorption sites identified for all of the surface intermediates. It is worthwhile to point out some general trends. As expected, highly coordinatively unsaturated adsorbates tend to favor 3- and 4-fold coordination sites, whereas less reactive adsorbates are preferentially located in bridge and top positions on the surface. For instance, C favors 4-fold coordination on the (100) facet below the step, whereas CH_3 is preferably adsorbed on top of the step-edge atom. The C_2 and oxygenated C_1 and C_2 fragments prefer to adsorb on the surface in a bidentate and, in some cases, tridentate manner, depending on the extent of hydrogenation of the C and O atoms.

To analyze the relative stabilities of the surface intermediates, we constructed a stability plot (Figure 4). All energies are given with respect to adsorbed atomic C, O, and H according to the formula.

$$E_{\mathrm{stab,rel}} = E_{\mathrm{ads}} - x(E_{\mathrm{C}}) - y(E_{\mathrm{H}}) - z(E_{\mathrm{O}}) + (x + y + z - 1)*E_{\mathrm{surf}} \quad (7)$$

where $E_{\mathrm{stab,rel}}$ is the relative stability, E_{ads} the electronic energy of the adsorbate on the surface, E_j the electronic energy of C,

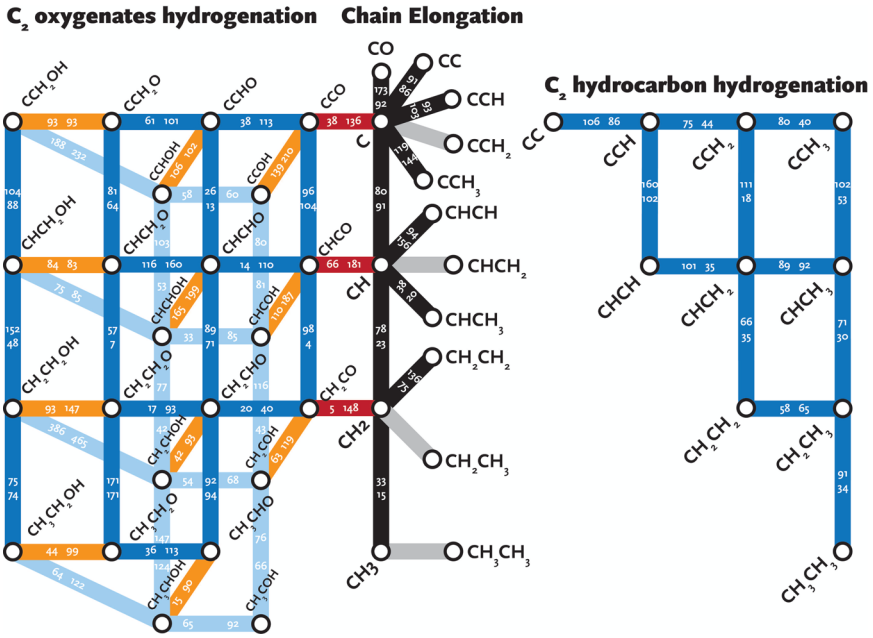

Figure 3. Forward and backward activation energies (in kJ/mol) for the formation of C_2 intermediates and products from CO. The central black axis shows C hydrogenation and CH_x + CH_y coupling reactions to generate C_2 hydrocarbons (black branches to the right) via hydrogenation and C_2 oxygenates (red branches to the left) by CH_x + CO coupling. Gray pathways represent reactions for which the transition state was not identified. The left and right diagrams show the interconnected hydrogenation reactions for C_2-oxygenates and C_2-hydrocarbons, respectively. Yellow and blue pathways represent (de)hydrogenation reactions of O and C atoms, respectively.

DOI: 10.1021/acscatal.5b01391
ACS Catal. 2015, 5, 5453−5467

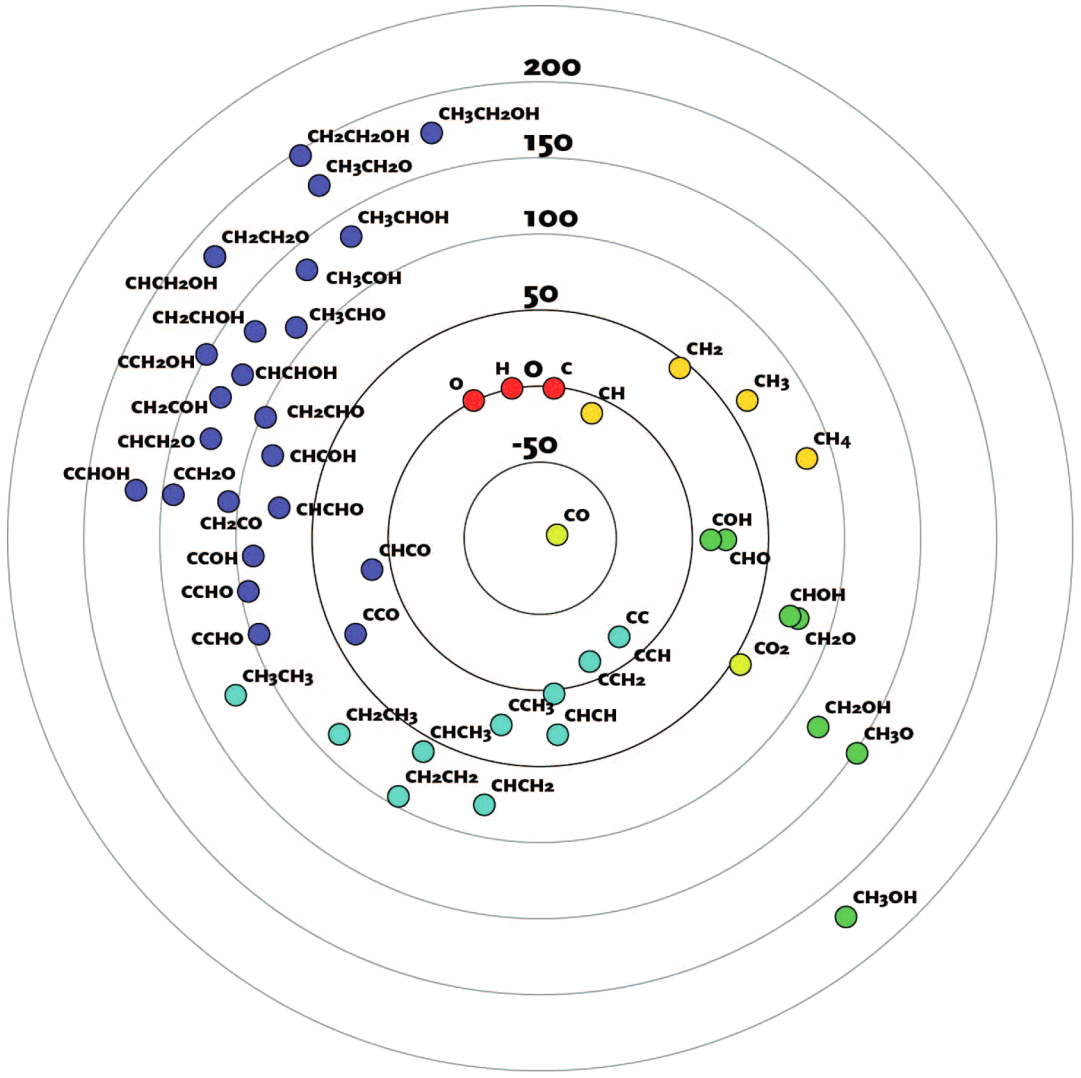

Figure 4. Stability plot of all surface reaction intermediates relevant to CO hydrogenation on the Rh(211) surface. Intermediates located closer to the center are more stable. The energy of each compound is calculated using atomic carbon, oxygen, and/or hydrogen adsorbed on the surface as the reference state (energies in kJ/mol). The different colors indicate the type of component (i.e., red for atomic adsorbates, yellow for C_1 alkanes, green for C_1-oxygenates, teal for C_2 alkanes, and blue for C_2 oxygenates) The azimuthal angle for the species follows the increasing degree of coordinative saturation.

H, or O in their most stable configurations on the surface, E_{surf} the electronic energy of an empty surface and x, y, z the number of atoms of C, H, or O constituting the adsorbate, respectively. All energies are in kJ/mol. Lateral interactions between adsorbates were ignored in this case. From this plot, it is immediately clear that CO is very stable on the surface. The dissociation of CO into the C_1 monomer is endothermic, which is consistent with the lower reactivity of Rh compared with Ru and Co, for which CO dissociation on stepped surfaces is exothermic. C and CH are much more stable surface species than CH_2 or CH_3. Accordingly, we can predict that C and CH species are the dominant CH_x surface species under reaction conditions. Oxygenated species are less stable on the surface than their oxygen-free counterparts (e.g., CC is more stable than CCO by about 50 kJ/mol). This difference relates to the relatively high stability of atomic O on the Rh(211) surface.

3.1.2. Direct and H-Assisted CO Dissociation. Direct and H-assisted CO dissociation reactions on the stepped Rh(211) surface have been extensively investigated before by us[24,28] and others.[22,34,51] To construct a consistent database of kinetic parameters for microkinetics simulations, we computed these elementary reaction steps at the same computational accuracy as employed for the other reaction steps. The activation barriers of the various CO dissociation reaction steps are tabulated in Table S2. Direct dissociation of CO with an activation barrier of 173 kJ/mol is preferred over H-assisted alternative pathways. The latter steps involve HCO and COH intermediates, whose formation is highly endothermic (93 and 103 kJ/mol, respectively). The consecutive C−O bond scission steps with barriers of 170 and 172 kJ/mol, respectively, are nearly as difficult as direct CO dissociation. Accordingly, H-assisted CO dissociation pathways have much higher overall barriers compared with direct CO dissociation. Thus, direct CO dissociation will be the dominant pathway for CO activation on Rh(211). The activation energy of 173 kJ/mol is substantially higher than values reported for the stepped surfaces of typical Fischer−Tropsch active transition metals such as Ru (65 kJ/mol)[26] and Co (92 kJ/mol).[52]

3.1.3. C Hydrogenation to CH_4. The forward and backward activation energies for the consecutive hydrogenation steps of

DOI: 10.1021/acscatal.5b01391
ACS Catal. 2015, 5, 5453−5467

adsorbed carbon to gaseous methane are given in Figure 2 and Table S3. The results are consistent with available data in the literature,[24] which are reported here for consistency. The hydrogenation steps of C to CH and CH to CH_2 have relatively high activation energies of 80 and 78 kJ/mol, respectively. The hydrogenation of CH to CH_2 is endothermic by 55 kJ/mol. Consecutive hydrogenation steps from adsorbed CH_2 to CH_3 and CH_3 to CH_4 have activation barriers of 33 and 50 kJ/mol, respectively. The former two hydrogenation steps occur along the stepped surface, whereas the latter two take place at the step-edge (see the SI for geometries). These results are similar to those of Cheng et al., who found that the first two hydrogenation steps have higher activation energies than the latter two. They also reported that CH formation is endothermic rather than exothermic, as found in the present study.[53] The C hydrogenation pathway to CH_4 is different from the one determined for the stepped Ru(11$\bar{2}$1) surface. For the Ru surface, only the first hydrogenation step to CH occurs along the step, and the other hydrogenation steps take place at the step-edge.[26]

3.1.4. CO Hydrogenation to Formaldehyde and Methanol. Adsorbed CO can be hydrogenated to formaldehyde and methanol by a sequence of hydrogenation steps. In total, we considered 10 different direct CO hydrogenation steps (Table S4). These reactions include hydrogenation reactions of the C or the O atom. The two reactions that lead to the formation of HCO and COH have already been discussed in section 3.1.2. The barriers for all of these elementary reaction steps are given in Figure 2; all CO hydrogenation steps are endothermic. The hydrogenation of HCO to methanol proceeds as follows. HCO initially bound in a bridged fashion by its C atom is hydrogenated at the step-edge with a relatively low barrier of 69 kJ/mol. The resulting H_2CO adsorbate migrates to the bottom of the step, where it is then bound to the surface by its C and O atoms. The forward barrier for hydrogenation of CH_2O to CH_3O is high (146 kJ/mol). CH_2O desorption is more favorable at 99 kJ/mol. For the CH_3O intermediate, the octet rule is fulfilled for the C atom; the binding of CH_3O preferentially occurs via the O atom at the step-edge to take advantage of the lower coordination number of the Rh step-edge atom. The final hydrogenation step to form methanol takes place with a forward reaction barrier of 60 kJ/mol, and the methanol desorption energy is 25 kJ/mol. An alternative pathway to methanol starts from COH. The associated reactions occur at the step-edge site. COH is adsorbed on an fcc site prior to hydrogenation. The hydrogenation of COH to HCOH has a forward barrier of 109 kJ/mol. The hydrogenation of CHOH to CH_2OH proceeds in a manner comparable with the hydrogenation of HCO to H_2CO; the respective forward barriers are 63 and 60 kJ/mol. The final hydrogenation step of CH_2OH to form methanol is very difficult (E_{act} = 183 kJ/mol). Overall, the methanol formation pathway that proceeds through CO hydrogenation via CH_3O (alkoxy route) is more favorable than the pathway via the hydrogenation of the COH intermediate (hydroxyl route). The data predict that formaldehyde will be a more likely product of direct CO hydrogenation than methanol.

3.1.5. CH_x + OH_y Coupling. A total of seven CH_x + OH_y coupling reactions were considered. Three of these coupling reactions are the reverse reactions of C−O bond cleavage reactions, namely, those for CO, HCO, and COH intermediates. The other coupling reactions are given in Table S5. All coupling reactions take place at the step-edge with the C atom bound to an Rh atom with a low coordination number of seven. The coupling proceeds via the migration of the OH_x adsorbate to the adjacent edge to form the C−O bond (see Figure S1). With the exception of CH + O coupling, all of the CH_x + OH_y coupling reactions are endothermic. The most facile coupling reaction is the one between CH_2 and O to form formaldehyde (E_{act} = 95 kJ/mol; reaction 21), followed by CH_2 + OH coupling (E_{act} = 118 kJ/mol; reaction 11). The result that CH_2 + O coupling is the most facile is in agreement with the literature.[22]

3.1.6. CH_x + CH_y Coupling. C_2-hydrocarbon formation by coupling of two C_1 species can proceed in ten different ways. We were able to identify the transition states of six of these coupling steps and they are shown in Table S6. For several candidate coupling reactions, we did not identify a transition state. In nearly all of these cases, the origin of this difficulty is related to the repulsive interactions between the two fragments. Although one cannot prove that such reactions are not possible, our investigations suggest that the associated barriers should be relatively high. All CH_x + CH_y coupling reactions take place at the step-edge site. To form a C−C bond, one of the two C_1 intermediates is adsorbed on the step at a 4-fold site, and the other C_1 species moves to an adjacent site (Figure S2). In the case of coupling with CH_3, the CH_3 fragment is no longer bound to the surface after coupling. The most facile of these coupling reactions is CH + CH_3, which has a barrier of only 38 kJ/mol. All the other coupling pathways have substantially higher activation barriers. Chen and Liu indicated that C + CH and CH_2 + CH_2 coupling reactions are preferred for C−C bond formation on the Rh(322) surface, which has a very similar topology as the Rh(211) surface.[34]

3.1.7. CH_x + CO Coupling. CO coupling to CH_x surface intermediates was studied in order to identify the pathways that lead to C_2-oxygenate formation. Table S7 lists the three relevant coupling reactions. CO coupling occurs either at the step-edge (C + CO coupling and CH_2 + CO coupling) or at the upper terrace (CO + CH coupling). The most facile CO insertion reaction is the one between C and CO with an activation barrier of 136 kJ/mol. Coupling reactions of CO with CH and CH_2 proceed with higher activation energies of 181 and 148 kJ/mol, respectively. Kapur et al. found that CH_2 + CO coupling has the lowest barrier;[22] these authors did not study the C + CO coupling reaction.

3.1.8. CH_xCH_y Hydrogenation. The formation of ethylene and ethane proceeds by a series of hydrogenation reactions after the formation of the C−C bond. In total, there are 12 unique hydrogenation steps (Table S8). The locations of these hydrogenation reactions depend on the number of hydrogen atoms attached to the carbon atoms of the reacting intermediates. For instance, ethyl hydrogenation takes place at the step-edge, whereas earlier hydrogenation steps occur along the step. With the exception of $CHCH_2$ hydrogenation to $CHCH_3$ and CH_2CH_2 hydrogenation to CH_2CH_3, all of these elementary reaction steps are endothermic and proceed with forward activation energies below 120 kJ/mol. The notable exception is CCH hydrogenation to CHCH, which has a barrier of 160 kJ/mol.

3.1.9. $CH_xCH_yO_z$ Hydrogenation. Acetaldehyde and ethanol can be formed by the hydrogenation of $CH_xCH_yO_z$ intermediates. There are 43 unique elementary reaction steps, and the corresponding forward and backward activation energies are listed in Table S9. Similar to CH_xCH_y hydrogenation, the majority of the $CH_xCH_yO_z$ hydrogenation steps

DOI: 10.1021/acscatal.5b01391
ACS Catal. 2015, 5, 5453−5467

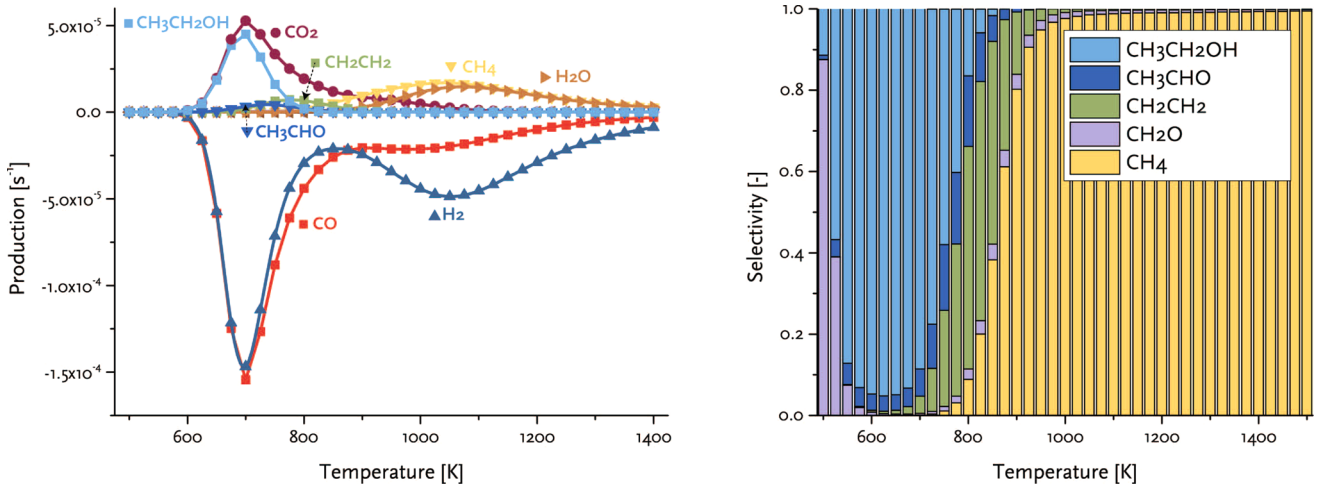

Figure 5. (left) Reaction rates (reactants negative, products positive) predicted by the microkinetics simulations of synthesis gas conversion on Rh(211) (p = 20 atm, H_2/CO ratio =2). (right) Carbon-based product selectivity as a function of temperature.

are endothermic. $CH_xCH_yO_z$ hydrogenation occurs either at the upper terrace or on the step-edge depending on the number of hydrogen atoms attached to the carbon atoms of the reacting intermediate. The majority of the hydrogenation reactions have activation barriers between 80 and 120 kJ/mol. It is worth noting that very high energy barriers are associated with the hydrogenation of CCO to CCOH (210 kJ/mol), CHCO to CHCOH (187 kJ/mol), CHCHO to CHCHOH (199 kJ/mol), CCHOH to CCH_2OH (232 kJ/mol), and CH_2CHOH to CH_2CH_2OH (465 kJ/mol).

3.1.10. Oxygen Removal. There are two routes for the removal of oxygen from the surface. The first one involves the formation of H_2O by hydrogenation of surface O adatoms. The second one is the oxidation of CO to CO_2. Water formation involves the hydrogenation of O to OH followed by direct hydrogenation of OH to H_2O or the alternative reaction of two OH groups to produce H_2O and an O atom (Table S10). The latter proton migration pathway is energetically preferred over hydrogenation of OH with H. The lower barrier for proton migration has also been reported for water formation on the stepped Ru(11$\bar{2}$1) surface.[26] The oxidation of CO by O occurs with a forward barrier of 130 kJ/mol; the backward barrier is 80 kJ/mol.

3.2. Microkinetics Simulations. *3.2.1. Overall Reaction Kinetics.* Microkinetics simulations predict the CO consumption rate and product distribution as a function of the reaction temperature. The kinetic parameters are based on the DFT-computed activation energies and pre-exponential factors. The pressure in our simulations is set at 20 atm, and the H_2 to CO ratio is 2. Figure 5a shows the normalized turnover frequencies for reactant (CO and H_2) consumption and product (hydrocarbons, CO_2 and H_2O) formation as a function of temperature. The optimum CO consumption rate occurs around 700 K. The decrease in the CO consumption rate at higher temperatures is caused by the rapid decrease of the surface CO coverage with temperature (see Figure S3 for the coverages as a function of temperature). The influence of the temperature on the hydrocarbon and oxygenate product distribution is shown in Figure 5b. We did not take into account CO_2 in reporting the product distribution. The product distribution including CO_2 formation is reported in Figure S3.[20,21] The preference for O removal by CO_2 at relatively low temperatures is consistent with experimental data.

At relatively low temperatures (T < 600 K), the dominant product is formaldehyde. This is because the CO dissociation barrier is higher than the barrier for CO hydrogenation to formaldehyde (*vide supra*). Methanol is not formed because the barrier for hydrogenation of formaldehyde to methanol is higher than the formaldehyde adsorption energy. With increasing temperature, the rate of CO dissociation increases. At the same time, ethanol selectivity strongly increases; small amounts of acetaldehyde are also formed. Optimum ethanol yield occurs at 700 K. At this temperature, the total yield of C_2-oxygenates (ethanol and acetaldehyde) is also the highest. At higher temperatures, the methane selectivity strongly increases at the expense of C_2-oxygenates. Ethylene is formed in small amounts at intermediate temperatures. Our simulations show that ethane is not formed under the given reaction conditions. Above 900 K, methane is the dominant product, and ethylene and formaldehyde appear as side-products. Oxygen is removed from the surface as CO_2 and formaldehyde at low temperature. (Figure S4). At intermediate temperatures, ethanol and acetaldehyde are the dominant products that remove O from the surface. At high temperatures, the rates of hydrogenation of C and O are so fast that exclusively methane and water are formed.

Experimental studies report very low selectivity to hydrocarbons with more than two C atoms during synthesis gas conversion on Rh catalysts.[20,21] We did not include the formation of paraffins and olefins with more than two carbon atoms in our microkinetics model. To determine whether this simplification was justified, we carried out additional simulations in which chain-growth reactions were included for hydrocarbons containing up to 5 C atoms. We considered two different pathways for C−C coupling. Growth by the carbide mechanism was invoked by using the kinetic parameters for the CH_x + CH_y coupling reactions to kinetically describe C−C bond forming steps for hydrocarbons with more than two C atoms (Table S6). We also included the CO insertion mechanism in our model (Table S11). The results of these simulations demonstrate that the selectivity of hydrocarbons with more than two C atoms was negligible under the given reaction conditions. The chain-growth probability for C_{2+}-hydrocarbons was estimated to be 10^{-7}. The low chain-growth rate is due to the high barrier for CH + CH coupling compared to C + CO coupling. With respect to the CO insertion

DOI: 10.1021/acscatal.5b01391
ACS Catal. 2015, 5, 5453−5467

mechanism, we found that the rate of C−O dissociation in R-CH_xCO intermediates was negligible. In contrast to Rh, Co and Ru produce significant amounts of long-chain hydrocarbons. For the stepped Ru surface, this difference is due to the much lower barrier for CH + CH coupling as compared with the barrier for CH_x + CO coupling.[26,27] The formation of ethylene as observed in our microkinetics simulations does not occur via CH + CH coupling but, instead, via CH_2 + CH_2 coupling. The barrier for this coupling reaction is lower than barriers for C + CO and CH + CH coupling. The reason why ethylene selectivity remains low in comparison to the other products is the relatively low CH_2 coverage, which relates to the low stability of CH_2 vs. C (Figure 4).

The steady-state surface coverages belonging to these simulations for the stepped Rh(211) surface are given in Figure S5. The surface is completely covered with CO at low temperatures. At intermediate temperatures, the rate of CO dissociation increases, because empty sites appear on the surface. The surface also contains H and O atoms and CH_x and CC fragments. At very high temperatures, the surface will be nearly empty. Comparison of reaction rates to experimental data is not possible given the accuracy of DFT-computed barriers. In general, the computed rates are lower than experimental values. This has two important reasons. First, the adsorption energies computed by DFT are generally overestimated. Second, we did not take into account lateral interactions that will also decrease the CO coverage and, hence, increase the CO dissociation rate. Nevertheless, the present data are consistent with activity and selectivity trends observed in the experimental literature. We use our analysis to provide detailed insight into the mechanism of a complex reaction in which selectivity issues play an important role. We compared computed kinetic parameters such as the reaction orders in CO and H_2 and the apparent activation energies to literature data. The temperature dependence of these kinetic parameters is given in the Supporting Information (Figure S6). The computed kinetic parameters lie within the range of values reported in literature for Rh-catalyzed CO hydrogenation.[21,54−57] The reaction order with respect to CO is negative because of the high CO coverage. The reaction order with respect to H_2 is positive. For instance, Levin et al.[57] reported experimental CO and H_2 reaction orders of −1.0 and 1.0, respectively, and an apparent activation energy of 110 kJ/mol. The negative CO reaction order is also predicted by our simulations and is due to the high CO coverage, which blocks the dissociation of CO as surface vacancies are needed. The CO reaction order becomes less negative with increasing temperature, because empty sites appear on the surface. At intermediate temperatures, the CO reaction order is positive because ethanol is the main reaction product in this regime and CO is needed to generate the CO-containing reaction intermediate. In the high-temperature limit, the CO reaction order is close to 0.5, and the reaction order with respect to H_2 is always above unity. These kinetic parameters indicate that CH_x hydrogenation steps are the rate-controlling steps for methane formation at high temperatures.

3.2.2. Importance of Step-Edge Sites. To elucidate the importance of the step-edge sites for CO dissociation and coupling reactions, we carried out additional microkinetics simulations involving DFT data for the less reactive Rh(111) surface. Kinetic data for CO dissociation on Rh(111) were taken from Filot et al.[28] Barriers for the elementary reaction steps that lead to methanol and ethanol for Rh(111) were taken from Choi and Liu.[9] The CO consumption rates computed for syngas conversion on the Rh(111) surface (Figure S7a and Table S12) are several orders of magnitude lower than those for the Rh(211) surface. This is due to the high overall CO dissociation barrier on the closed-packed surface. The main reaction products on Rh(111) were formaldehyde and methanol. We found that on Rh(111) methanol formation competes with formaldehyde desorption. This is different from the result for Rh(211) where formaldehyde desorption was favored over methanol formation. Because the CO dissociation barrier on Rh(100) is also much higher than on the step-edge site,[28] we predict that CO will also only be hydrogenated on this more open terrace surface.

We then carried out microkinetics simulations on a hypothetical surface using kinetic data for the Rh(111) surface for CO dissociation and C hydrogenation[24] and, for all other coupling and hydrogenation steps, the data for the Rh(211) surface determined in the present study. Expectedly, the CO consumption rates were also very low in this case, and formaldehyde and water were the main reaction products (Figure S7b and Table S13). This result shows that the step-edge sites are essential for CO dissociation. Without facile CO dissociation, CO can only be hydrogenated to formaldehyde and methanol.

A next set of simulations was done to evaluate the importance of step-edge sites for the coupling reactions. For this purpose, we constructed a model in which CO can easily dissociate by using kinetic data for the Rh(211) data; all coupling and hydrogenation steps that will lead to methane, methanol, and ethanol are based on DFT data for the Rh(111) surface[28] (Figure S7c). The CO dissociation rate of this hypothetical surface is much higher as compared with the Rh(111) surface, because a low CO dissociation barrier was used. The main reaction products were formaldehyde and methanol at low temperature and methane at high temperature. Ethanol was not observed in these simulations. These findings convincingly demonstrate that the step-edge sites are important for the formation of ethanol at intermediate temperatures, because they can catalyze (i) CO dissociation at conditions where the surface contains adsorbed CO and (ii) the CH_x + CO coupling reactions that lead to C_2-oxygenates.

3.2.3. Reaction Network Analysis: Rate and Selectivity Control. In this section, we discuss in detail the reaction network that leads to the various C-containing reaction products. In particular, we will identify elementary steps that control the overall CO consumption rate and the product selectivity. We will investigate how these steps change with reaction temperature. The elementary reaction steps that control the rate of CO consumption and the formation of the various products are identified by determining the degree of rate control (DRC) for each elementary reaction step.[41] The DRC of a chemical reaction is defined as the relative change of the rate as a result of the relative change in the rate constant of a particular elementary reaction step while keeping the equilibrium constant the same:

$$\chi_{c,i} = \left(\frac{\partial r_c / r_c}{\partial k_i / k_i}\right)_{k_{j\neq i}, K_i} = \left(\frac{\partial \ln(r_c)}{\partial \ln(k_i)}\right)_{k_{j\neq i}, K_i} \quad (8)$$

In eq 8, $\chi_{c,i}$ is the DRC parameter of elementary reaction step i for key component (i.e., a reactant or product) c, r_c is the overall reaction rate for key component c, and k_i and K_i are the forward rate and equilibrium constants for the elementary

DOI: 10.1021/acscatal.5b01391
ACS Catal. 2015, 5, 5453−5467

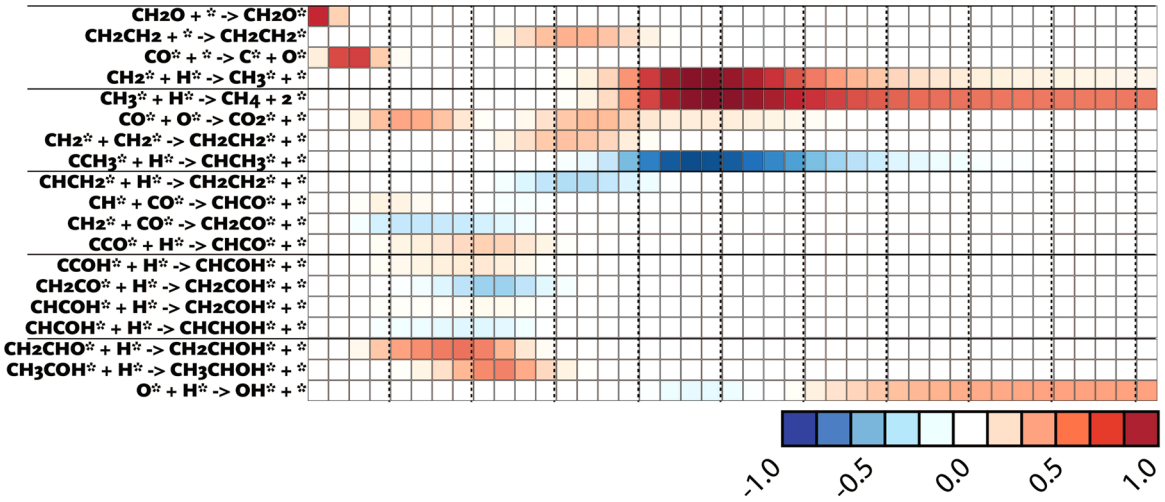

Figure 6. Degree of rate control for the CO consumption rate as a function of temperature for the Rh(211) surface (only reactions with an absolute DRC value greater than 0.1 are shown).

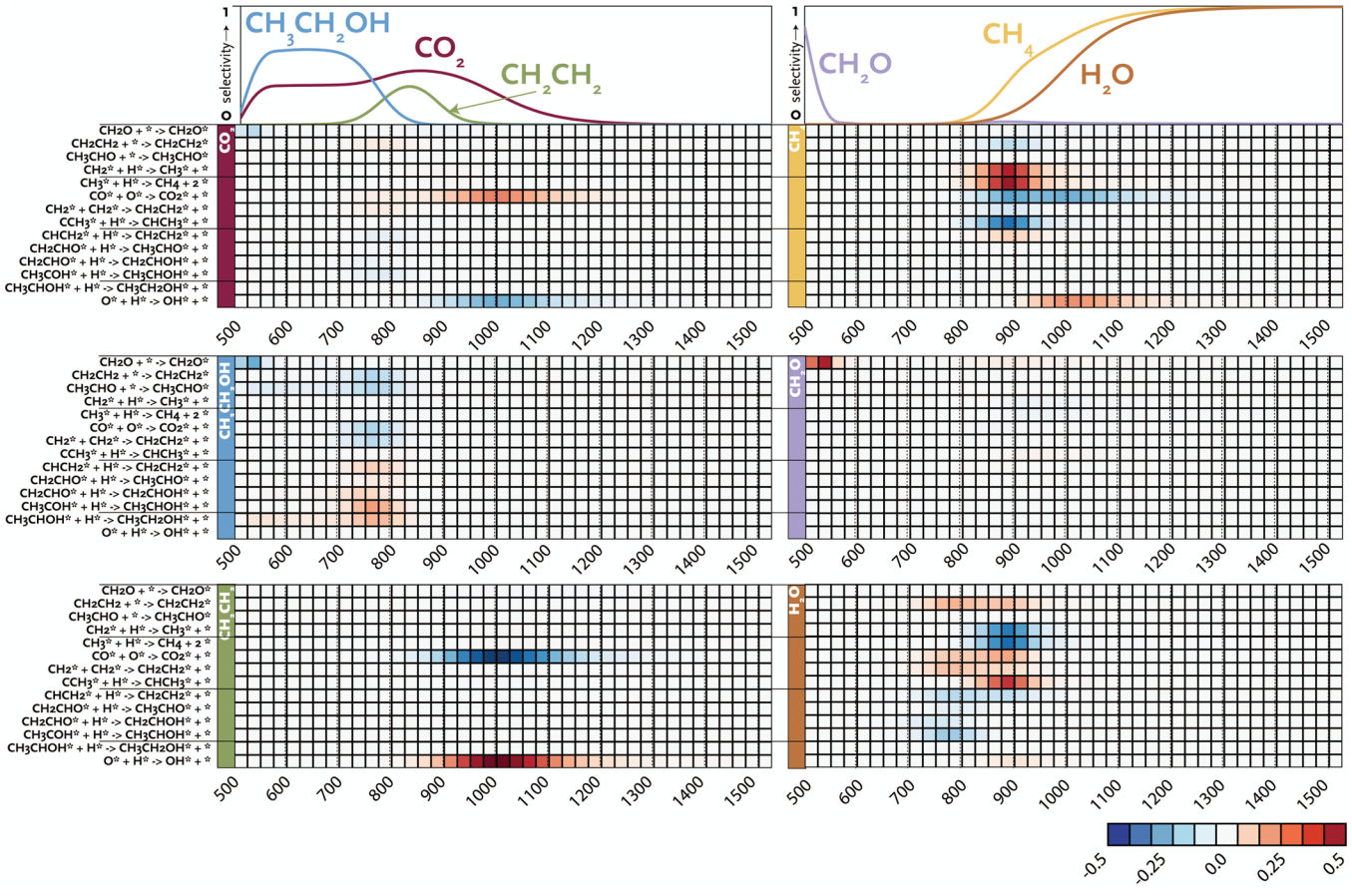

Figure 7. Degree of selectivity control for all products as a function of temperature. For clarity, the selectivity of a particular product is also given as a function of temperature at the top of the table (data for acetaldehyde in Supporting Information).

reaction step *i*, respectively. The condition that the equilibrium constant does not change implies that only the location of the transition state of a particular step is changed on the potential energy surface, which affects the forward and backward rate constants. The sum of all DRC values is unity.[41] One may determine DRC values for the consumption rate of any one of the reactants, or the production rate of any one of the products. A positive DRC value for a particular elementary reaction step indicates that this step limits the reaction rate. A decrease in the activation energy for the transition state of this elementary reaction step would increase the overall rate. Negative values, on the other hand, point to rate-inhibiting elementary reaction steps. Lowering the barrier of such a reaction step decreases the overall reaction rate.

As we are mainly interested in selectivity issues for synthesis gas conversion on Rh nanoparticle catalysts, we employ the degree of selectivity control (DSC).[42] The DSC quantifies the extent to which a particular elementary reaction step influences

DOI: 10.1021/acscatal.5b01391
ACS Catal. 2015, 5, 5453−5467

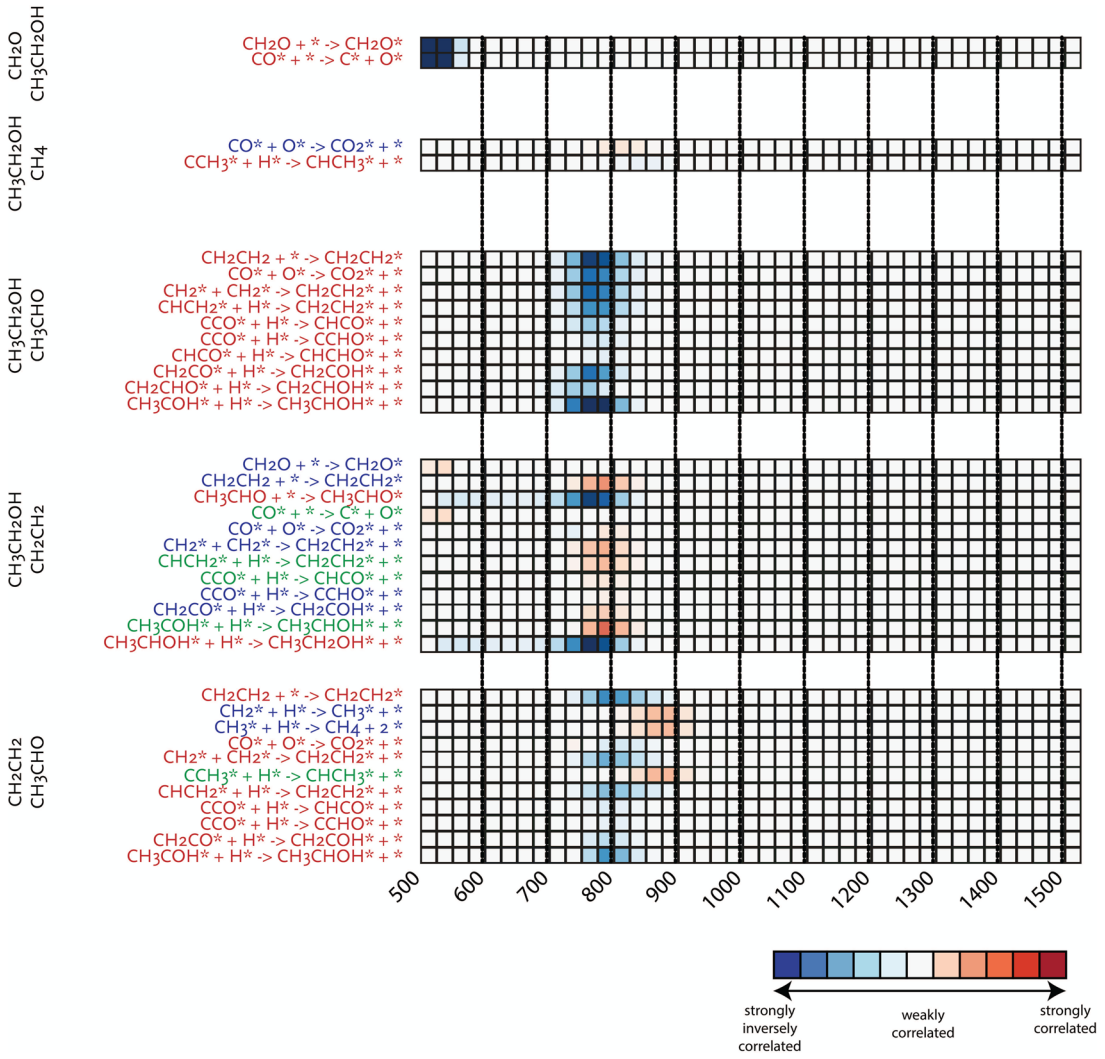

Figure 8. Degree of selectivity control correlations between ethanol and other competing products. A complete overview is given in the Figure S9. Elementary reaction steps are color-coded according to their influence on the product selectivities. A red elementary reaction step points to an opposite effect between the two products, green indicates that the products have a common rate-controlling reaction, and blue indicates that the two products have a common rate-inhibiting step.

the selectivity to certain products. We determine the sensitivity of the absolute change in selectivity as a result of the relative change in the rate constant of a particular elementary reaction step. We use the absolute instead of the relative change, because we are interested in understanding selectivity issues (i.e., in case of competition in the formation of two products). The degree of selectivity control for a particular key component is defined in the following manner:

$$\varepsilon_{c,i} = \left(\frac{\partial \eta_c}{\partial k_i / k_i}\right)_{k_{j\neq i}, K_i} = \left(\frac{\partial \eta_c}{\partial \ln(k_i)}\right)_{k_{j\neq i}, K_i} \tag{9}$$

where $\varepsilon_{c,i}$ is the DSC of product c due to a change in the kinetics of elementary reaction step i, and η_c is the selectivity of a key product component. We again impose that the equilibrium constant of the considered elementary reaction step does not change. The products considered in the present study are carbon dioxide, methane, formaldehyde, ethanol, acetaldehyde, water and ethylene. One can rewrite eq 9 in such way that the DSC can be determined directly from the DRC values of the reactant and the relevant product (derivation in the Supporting Information):

$$\varepsilon_{c,i} = \eta_c(\chi_{c,i} - \chi_{\text{reactant},i}) \tag{10}$$

In the present study, we always base the DSC calculations on CO as the reactant.

DRC values based on CO as the key reactant are shown as a function of temperature in Figure 6. The DSC values for the products are listed in Figure 7. For clarity, Figure 7 also contains the selectivity for each product as a function of temperature. The DRC values based on the products used to compute the DSC values are given in the Supporting Information (Figures S8). In Figure 6, we show the most important elementary reaction steps for CO conversion. Figure 7 only reports the elementary reaction steps with DRC and DSC values greater than 0.01. A total of 45 elementary reaction steps are relevant to the discussion of rate and selectivity control.

We first illustrate the use of these parameters in the low-temperature regime (500−600 K), in which there is a change in the selectivity from exclusively formaldehyde to predominantly

DOI: 10.1021/acscatal.5b01391
ACS Catal. 2015, 5, 5453−5467

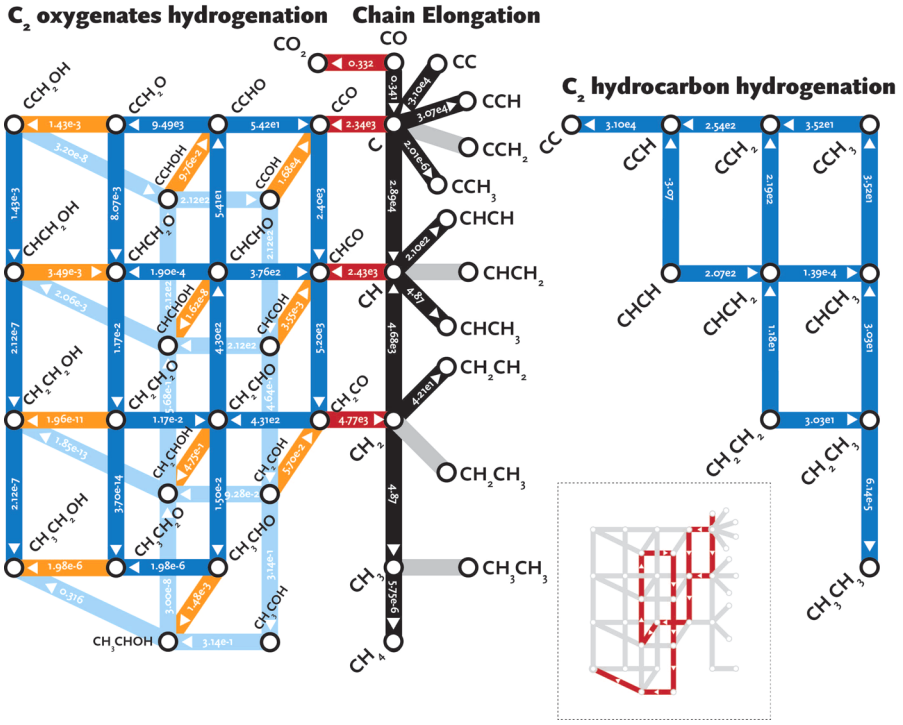

Figure 9. Reaction pathways for synthesis gas conversion to ethanol on Rh(211) (p = 20 atm, T = 700 K, H_2/CO ratio = 2). The numbers in the arrows are molar reaction rates (s^{-1}) and are normalized with respect to the amount of adsorbed CO. The network in the box shows the dominant ethanol formation pathway.

ethanol. Figure 6 and 7 show that, at temperatures below 600 K, formaldehyde desorption and CO dissociation control the overall CO consumption rate. Our simulations predict that methanol is not formed due to the high barrier for the hydrogenation of adsorbed CH_2O, that is to say, desorption of CH_2O is preferred over its hydrogenation. Experimentally, methanol is observed as the dominant C_1-oxygenate product.[58] We expect that formaldehyde can readsorb on other less reactive surface planes, where it can be easily hydrogenated in keeping with the results of the simulations for the Rh(111) surface. Figure 7 shows that at low temperature there is competition between formaldehyde and CO_2. When the temperature is too low for efficient CO dissociation, formaldehyde is the dominant product. When the temperature reaches 550 K, CO dissociation becomes feasible and CO_2 is formed by the CO + O reaction. Note the sum of the DSC values of all elementary reaction steps for a single product equals zero.

The selectivity shifts from formaldehyde to ethanol, when the temperature is increased from 525 to 600 K. In this regime, the DSC values for CH_2O formation are positive, while the DSC value for CO dissociation is negative. The DSC values for each of these two elementary reaction steps are strongly and inversely correlated for CH_2O vs. ethanol formation in this temperature regime. This can be understood in the following way. When, on the one hand, formaldehyde desorbs more easily (decrease of the CH_2O desorption energy), ethanol selectivity decreases because CH_2O formation consumes CO from the surface needed for the formation of the CCO intermediate that leads to ethanol (see below). When, on the other hand, the CO dissociation is made more facile, CO is converted to C, which can couple to CO to form CCO, which is the precursor to ethanol.

The above shows that it is useful to identify elementary reaction steps for which the DSC parameters of two particular products are correlated. For this purpose, we define a correlation coefficient $\rho_{c1,c2,i}$ that is based on the DSC parameters of two products c_1 and c_2 for a particular reaction step i in the following manner:

$$\rho_{c1,c2,i} = -\varepsilon_{c1,i}\cdot\varepsilon_{c2,i} \tag{11}$$

Based on the 7 products considered in the present study, we need to compute 21 different correlation coefficients for every elementary reaction step. Again, we limit ourselves to those reactions that have correlation coefficients larger than 0.01. As we correlate DSC values that are smaller than unity, only few steps have correlation coefficients greater than 0.01. The resulting data are presented in Figure 8. For the case of CH_2O versus CH_3CH_2OH formation, we see that the two reaction steps discussed above lead to negative correlation coefficients. A negative correlation coefficient implies that the elementary reaction step under consideration controls the formation of the two products in a competitive manner. This competition is controlled by the concentration of a common reaction intermediate. As we will show below, there are two further cases to be considered. In both cases, the correlation is positive, indicating that the changes in selectivity of the two considered products caused by a change in the kinetics of a particular elementary reaction step are in the same direction. There are two possibilities: lowering the barrier of a particular reaction step may either cause a decrease in the selectivity of the two products (indicated in blue in Figure 8) or an increase in the selectivity of both products (indicated in green in Figure 8).

We will use these DRC and DSC values along with the DSC correlations to discuss three regimes characterized by (I) selective ethanol formation (675−725 K); (II) the transition from selective ethanol formation to selective methane

DOI: 10.1021/acscatal.5b01391
ACS Catal. 2015, 5, 5453−5467

formation (725−900 K); and (III) selective methane formation (900 K and higher).

Regime I: Selective Ethanol Formation (675−725 K). Figure 9 shows the reaction network for ethanol formation. The molar rates are given for a reaction temperature of 700 K, which is the optimum temperature for the C_2-oxygenates selectivity. Adsorbed CO is dissociated into C and O adatoms. The contribution of H-assisted CO dissociation pathways involving CHO or COH surface intermediates is negligible under these conditions. There are two important CH_x + CO coupling steps, namely, C + CO and CH + CO, respectively, yielding adsorbed CCO and CHCO intermediates. Ethanol formation involves a complex series of surface reactions. First, CCO is hydrogenated to CH_2CHOH via CHCO, CHCHO, and CH_2CHO. The CH_2CHOH surface fragment is dehydrogenated to CHCHOH, CCHOH, and then to CCOH. Ethanol is then obtained by the sequential hydrogenation of CCOH to CHCOH, CH_2COH, CH_3COH, CH_3CHOH, and finally CH_3CH_2OH. The preference for this particular reaction sequence can be explained as follows. The O atom in adsorbed CCO is very strongly bound to the surface; the activation energy for its hydrogenation to CCOH is higher than 200 kJ/mol. When the two C atoms in CCO are partially hydrogenated, the O atom will be less strongly bound with the consequence that the O atom can be more easily hydrogenated. The activation barrier for O hydrogenation in adsorbed CH_2CHO is lower than 100 kJ/mol. When CCOH is obtained, the terminal C atom is first hydrogenated. The resulting CH_3COH intermediate only binds to the surface via the carbonyl C atom; this intermediate is then hydrogenated to adsorbed ethanol, whose desorption only costs 15 kJ/mol.

Figure 6 shows that the following elementary reaction steps control the rate of CO consumption (in decreasing order of DRC values): CH_2CHO hydrogenation to CH_2CHOH > CH_3COH hydrogenation to CH_3CHOH > CCO hydrogenation to CHCO > CO + O to CO_2. Oxygen removal by CO oxidation is slow because of the strong binding of the O adatom to the stepped surface. The overall CO consumption rate increases when O or other intermediates that lead to ethanol are removed, because more empty surface sites facilitate the dehydrogenation reactions in the reaction sequence of CCO to ethanol. Rate-inhibiting reactions also occur. For example, CH_2 + CO → CH_2CO inhibits the reaction rate, because lowering the barrier of this step leads to the decomposition of the CH_2CO intermediate. This shifts the CHCO + H ⇆ CH_2CO equilibrium to the right-hand side, resulting in a decrease of the CHCO coverage. CHCO is an important reaction intermediate in the formation of ethanol.

Detailed inspection of the molar fluxes in the reaction network shown in Figure 9 reveals that there are many surface reactions that occur at much higher rates than the overall CO consumption rate. For example, the rate of CH_2CO dissociation to CH_2 and CO is 4 orders of magnitude higher than the rate of CO consumption. Likewise, adsorbed C reacts with CH at high rate followed by its dehydrogenation to CC and the dissociation of the CC intermediate back to two C adatoms. The DRC values for these surface reactions are negligible. These reactions are not relevant to the formation of the product (ethanol in this temperature regime), because they react back to the C and CO surface species in a series of elementary reaction steps. Accordingly, we call these reactions spectator reactions in analogy with spectator species, which are present on the catalytic surface, yet are not directly involved in product formation. It should be stressed that the steady-state surface coverages of CCH and CC are low compared with the coverages of adsorbed C and CH.

Regime II: Transition from Selective Ethanol to Selective Methane Formation (725−900 K). The increase of the temperature from 725 to 900 K leads to an increase of the methane selectivity at the expense of ethanol. The increasing methane selectivity goes together with increasing ethylene and acetaldehyde selectivity. The competition between ethanol and methane is of particular interest, because it is experimentally observed that methane is the main competing product in ethanol production during synthesis gas conversion on Rh-based catalysts.[58] The shift in product selectivity occurs together with a shift in the rate-controlling steps going from regime I to regime III. Figure 8 shows that the CCH_3 + H → $CHCH_3$ reaction controls the product selectivity in the 750−850 K temperature range. Lowering the barrier of this step facilitates ethanol formation, because dehydrogenation of the $CHCH_3$ intermediate formed upon CH + CH_3 coupling results in CC, which can decompose into two C atoms. This pathway captures CH_3 species that would otherwise be hydrogenated to CH_4. The CCH_3 + H → $CHCH_3$ reaction step also exhibits a negative DSC correlation with ethylene and methane, because ethylene formation is also favored by the conversion of $CHCH_3$ to two C species as ethylene is mainly formed by direct coupling of two CH_2 species.

Our analysis reveals that there is no possibility to change the selectivity between ethanol and ethylene, as there are no nonzero correlation coefficients for the elementary reaction steps. On the contrary, there are two reactions that predominantly control the ethanol selectivity compared with that of acetaldehyde. The ethanol selectivity increases when the energy of the transition state for CH_3CHOH hydrogenation to CH_3CH_2OH is lowered. This hydrogenation step precedes ethanol desorption; if it is made more difficult, the selectivity to acetaldehyde increases. The acetaldehyde selectivity also increases when the desorption energy for acetaldehyde decreases, which negatively affects ethanol selectivity.

Acetaldehyde and ethylene formation compete predominantly with each other by their respective desorption reactions and, to a lesser extent, by the coupling of two CH_2 moieties (favoring ethylene formation) or by the hydrogenation steps of CH_xCOH_y (favoring acetaldehyde formation). Furthermore, we can see from Figure 8 that lowering the hydrogenation barrier of CH_2 and CH_3 results in lower acetaldehyde and ethylene formation as this results in higher methane selectivity, whereas lowering the $CHCH_3$ dehydrogenation barrier results in higher selectivity of both acetaldehyde and ethylene.

Regime III: Selective Methane Formation (900 K and above). At temperatures above 900 K, methane is the dominant reaction product. Ethylene and acetaldehyde are formed in small amounts. The rate-controlling steps are CH_2 and CH_3 hydrogenation. This is in line with the reaction orders discussed above. The hydrogenation reaction of CCH_3 to $CHCH_3$ is rate-inhibiting, because this elementary reaction step facilitates the production of ethylene at the expense of CH_4 formation. The reaction network is analyzed in more detail in Figure 10. The complete data are given in the Supporting Information (Figures S10). Methane is formed by direct CO dissociation followed by sequential hydrogenation of the C intermediate. Figure S8 shows the expected result that none of the C_1-oxygenate pathways are relevant for methane formation. Figure S10 shows that under conditions of predominant methane formation, the

DOI: 10.1021/acscatal.5b01391
ACS Catal. 2015, 5, 5453−5467

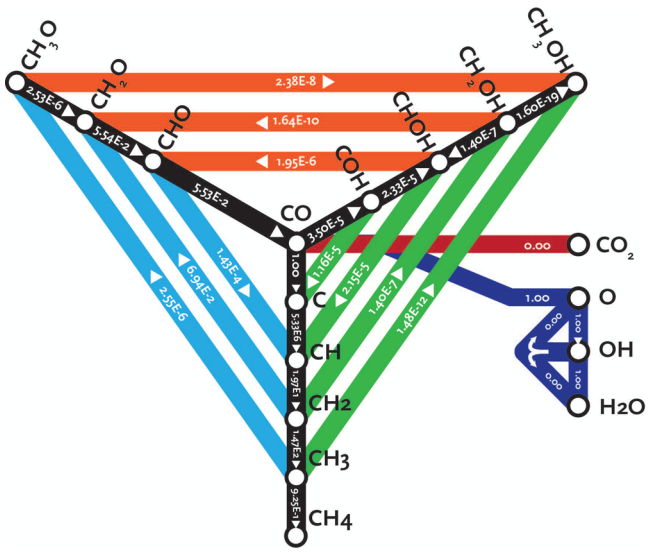

Figure 10. Reaction pathways for synthesis gas conversion to methane on Rh(211) (p = 20 atm, T = 1000 K, H_2/CO ratio = 2). Only the relevant elementary reaction steps leading to formation of methane are shown. The numbers in the arrows are molar reaction rates (s^{-1}) and are normalized with respect to the amount of adsorbed CO.

rate of C + CO coupling remains high compared with the overall CO consumption rate. These reactions do not lead to ethanol formation because of the high rates of CHCO and CH_2CO dissociation to CH_x and CO as well as the endothermicity of the hydrogenation reactions of CH_xCO intermediates that would result in ethanol.

3.2.3. General Discussion. The present study provides new insights into the mechanism of synthesis gas conversion on Rh nanoparticle catalysts. A key finding of these first-principles microkinetics simulations is that CO dissociation is not controlling the overall CO consumption rate on the stepped Rh(211) model surface under conditions that ethanol is the main product. Nevertheless, the CO consumption rate will scale with the number of step-edge sites, because CO dissociation will only occur at appreciable rate at such sites. This contrasts the suggestion made in many studies that slow CO dissociation is the main cause for ethanol formation on Rh catalysts.[14,15,33,58] At temperatures below 600 K, the dominant product is formaldehyde, because the rate of CO dissociation is low. Desorption of formaldehyde is preferred over hydrogenation to methanol on the stepped surface. On less reactive planar surfaces of Rh such as the close-packed (111) surface, the hydrogenation to methanol is easier. The key step that determines this selectivity is the hydrogenation of CH_2O to CH_3O. This step has a lower barrier on the Rh(111) surface (72 kJ/mol)[9] than on the Rh(211) surface (112 kJ/mol). Therefore, on a terrace surface on which CO dissociation barrier will not occur, methanol formation is the preferred product as confirmed by our microkinetics simulations for the close-packed surface. Experimental work of Hanaoke et al. for silica-supported Rh nanoparticles showed that the methanol selectivity strongly increased with decreasing Rh nanoparticle size.[58] This can be explained by the lower stability of step-edges on smaller particles. As a consequence, the surface of nanoparticles will contain a higher ratio of close-packed surface sites over step-edge sites such that the rate of CO dissociation decreases and the methanol selectivity increases. It is in line with the decreased CO dissociation rate observed for smaller particles.[58]

Regarding the selectivity to products with more than one C atom, our simulations correctly predict that high C_2-oxygenates selectivity is obtained at intermediate reaction temperatures. This is due to the lower barrier for C + CO coupling (136 kJ/mol) compared with the barrier of 156 kJ/mol for CH + CH coupling. This also explains why Rh does not produce higher hydrocarbons. Ethylene is nearly exclusively formed via CH_2 + CH_2 coupling. These data explain the low higher hydrocarbons selectivity observed in experimental studies.[21,55−57] In comparison, the CH + CH coupling reaction is kinetically favored over C + CO coupling on the step-edge site of Ru($11\bar{2}1$). Thus, we can conclude that the selectivity difference between Ru and Rh is because the step-edges of Ru catalyze CH + CH (and CH + CR, with R being an alkyl group) coupling reactions toward long-chain hydrocarbons[26,27] and the step-edges of Rh catalyze the formation of ethanol via C+CO coupling. The barriers for the cleavage of the C−O bonds in CH_xCO intermediates are very high (E_{act} > 180 kJ/mol). The consequence is that chain growth via the CO insertion mechanism is kinetically hindered. As discussed above, the chain-growth probability via CH_x insertion reactions (carbide mechanism) is also very low.

The CCO intermediate will undergo a complex sequence of hydrogenation and dehydrogenation steps that eventually lead to ethanol. Some of these hydrogenation reactions show a DRC value greater than zero. Also CO oxidation and O hydrogenation control the formation rate of ethanol at lower and higher temperature, respectively. This is because empty sites are required for the dehydrogenation reactions in the sequence from CCO to ethanol. The simulation data predict high ethanol selectivity at intermediate reaction temperatures. In experimental studies (see for instance the work of Hanaoke et al.[27,59]), the ethanol selectivity is usually much lower and methane is the dominant reaction product. We speculate that this is due to the rapid hydrogenation of CH_x surface intermediates that migrate to less reactive surface planes of Rh nanoparticles. Although the migration is thermodynamically unfavorable because of the weaker binding of the C atom to the close-packed surface compared with the step-edge, the overall barrier to hydrogenate this weaker bonded C atom to CH_4 will be lower on the closed-packed surface.

At higher temperatures, the CO consumption rate increases because of the decreasing surface coverage and increasing rate constant for CO dissociation; methane formation starts to compete with ethanol production. Ethylene, formaldehyde, and acetaldehyde are side-products. The higher hydrocarbons selectivity remains negligible at these temperatures. This is the regime that is relevant to many experimental studies.[27,59] Our kinetic analysis shows that $CHCH_3$ dehydrogenation controls the selectivity to ethanol. This provides a guiding principle for the design of Rh catalysts with improved ethanol selectivity. An increase in the C bond strength will lower the rate of $CHCH_3$ hydrogenation, resulting in increased ethanol selectivity.

4. CONCLUSIONS

The first-principles microkinetics model presented herein shows how ethanol is formed during synthesis gas conversion on a stepped Rh surface. Methane, ethylene, ethane, formaldehyde, methanol, and acetaldehyde are the other reaction products in this reaction, next to carbon dioxide and water. The reaction network and the elementary reaction steps that control

DOI: 10.1021/acscatal.5b01391
ACS Catal. 2015, 5, 5453−5467

the rate and the product distribution were analyzed as a function of the temperature. This work provides detailed insights into the complex nature of the surface reactions that leads to the various products as well as the competition between these products. We introduced a new concept based on the correlation between degrees of selectivity control of two products; this concept helps to identify the elementary reaction steps that most significantly control product selectivity.

The CO dissociation reaction takes place on the Rh(211) surface, because the CO dissociation barriers on the terrace surfaces of Rh are too high. The model predicts formation of formaldehyde at low temperature, ethanol at intermediate temperature, and methane at high temperature. At low temperature, formaldehyde is the main product, because the rate of CO dissociation is low. At intermediate temperatures, ethanol is formed by C + CO and CH + CO coupling followed by its hydrogenation to acetaldehyde and ethanol. The C + CO and CH + CO coupling reactions are preferred over CH_x + CH_x coupling reactions on the stepped Rh surface, which explains the high ethanol selectivity. A small amount of ethylene is formed by CH_2 + CH_2 coupling. Longer hydrocarbon chains with three or more C atoms are not formed because of the preference for C + CO coupling over CH_x + CH_y coupling and the high barrier for C−O bond cleavage in CH_xCO surface intermediates. Our finding show that the step-edge sites are essential to maintain a high enough rate of CO dissociation and to facilitate the coupling reactions for ethanol formation. At high temperature, C is rapidly hydrogenated to methane.

The microkinetics simulations show that, at intermediate temperatures, ethanol formation competes with methane formation. The rate-controlling steps are direct O removal, which is required to create empty sites to enable the dehydrogenation steps in the reaction sequence leading to ethanol, and CH_xCH_yO hydrogenation steps for ethanol formation. The most important reaction step that controls the selectivity for ethanol versus that of methane is $CHCH_3$ dehydrogenation.

■ ASSOCIATED CONTENT

Supporting Information

The Supporting Information is available free of charge on the ACS Publications website at DOI: 10.1021/acscatal.5b01391.

Geometries of the initial, transition, and final states of all elementary reaction steps; kinetic parameters as a function of temperature for synthesis gas conversion on Rh(211); derivation of the degree of selectivity control; figures for the degree of rate and selectivity control for all products (PDF)

■ AUTHOR INFORMATION

Corresponding Author

*E-mail: e.j.m.hensen@tue.nl.

Notes

The authors declare no competing financial interest.

■ ACKNOWLEDGMENTS

E.J.M.H. acknowledges financial support through the NWO-TOP grant provided by The Netherlands Organization for Scientific Research. The authors also thank The Netherlands Organization for Scientific Research for access to the national high-performance computing facilities.

■ REFERENCES

(1) Colley, S. E.; Copperthwaite, R. G.; Hutchings, G. J.; Terblanche, S. P.; Thackeray, M. M. *Nature* **1989**, *339* (6220), 129−130.
(2) van Santen, R. A.; Ciobîcă, I. M.; van Steen, E.; Ghouri, M. M. *Adv. Catal.* **2011**, *54*, 127−187.
(3) Higman, C.; Tam, S. *Chem. Rev.* **2013**, *114* (3), 1673−1708.
(4) Bezemer, G. L.; Bitter, J. H.; Kuipers, H. P. C. E.; Oosterbeek, H.; Holewijn, J. E.; Xu, X.; Kapteijn, F.; van Dillen, A. J.; de Jong, K. P. *J. Am. Chem. Soc.* **2006**, *128* (12), 3956−3964.
(5) den Breejen, J. P.; Radstake, P. B.; Bezemer, G. L.; Bitter, J. H.; Frøseth, V.; Holmen, A.; Jong, K. P. d. *J. Am. Chem. Soc.* **2009**, *131* (20), 7197−7203.
(6) Loveless, B. T.; Buda, C.; Neurock, M.; Iglesia, E. *J. Am. Chem. Soc.* **2013**, *135* (16), 6107−6121.
(7) Markvoort, A. J.; van Santen, R. A.; Hilbers, P. A. J.; Hensen, E. J. M. *Angew. Chem., Int. Ed.* **2012**, *51*, 9015−9019.
(8) Spivey, J. J.; Egbebi, A. *Chem. Soc. Rev.* **2007**, *36*, 1514.
(9) Choi, Y.; Liu, P. *J. Am. Chem. Soc.* **2009**, *131* (36), 13054−13061.
(10) Lu, J.; Liu, Y.; Li, N. *J. Nat. Gas Chem.* **2011**, *20* (4), 423−427.
(11) Wang, H.; Liu, J.; Fu, J.; Wan, H.; Tsai, K. *Catal. Lett.* **1992**, *12* (1−3), 87−96.
(12) Bhasin, M. M.; Bartley, W. J.; Ellgen, P. C.; Wilson, T. P. *J. Catal.* **1978**, *54* (2), 120−128.
(13) Pan, X.; Fan, Z.; Chen, W.; Ding, Y.; Luo, H.; Bao, X. *Nat. Mater.* **2007**, *6* (7), 507−511.
(14) Bowker, M. *Catal. Today* **1992**, *15* (1), 77−100.
(15) Chen, G.; Guo, C.-Y.; Huang, Z.; Yuan, G. *Chem. Eng. Res. Des.* **2011**, *89* (3), 249−253.
(16) Basu, P.; Panayotov, D.; Yates, J. T. *J. Am. Chem. Soc.* **1988**, *110* (7), 2074−2081.
(17) Zhang, Z. L.; Kladi, A.; Verykios, X. E. *J. Catal.* **1995**, *156* (1), 37−50.
(18) Wong, T. T. T.; Stakheev, A. Y.; Sachtler, W. M. H. *J. Phys. Chem.* **1992**, *96* (19), 7733−7740.
(19) Anderson, J. A.; Khader, M. M. *J. Mol. Catal. A: Chem.* **1996**, *105* (3), 175−183.
(20) Benedetti, A.; Carimati, A.; Marengo, S.; Martinengo, S.; Pinna, F.; Tessari, R.; Strukul, G.; Zerlia, T.; Zanderighi, L. *J. Catal.* **1990**, *122* (2), 330−345.
(21) Underwood, R. P.; Bell, A. T. *Appl. Catal.* **1986**, *21* (1), 157−168.
(22) Kapur, N.; Hyun, J.; Shan, B.; Nicholas, J. B.; Cho, K. *J. Phys. Chem. C* **2010**, *114* (22), 10171−10182.
(23) Mavrikakis, M.; Bäumer, M.; Freund, H. J.; Nørskov, J. K. *Catal. Lett.* **2002**, *81* (3−4), 153−156.
(24) Zhu, T. W.; van Grootel, P. W.; Filot, I. A. W.; Sun, S. G.; van Santen, R. A.; Hensen, E. J. M. *J. Catal.* **2013**, *297*, 227−235.
(25) Grabow, L. C.; Mavrikakis, M. *ACS Catal.* **2011**, *1* (4), 365−384.
(26) Filot, I. A. W.; van Santen, R. A.; Hensen, E. J. M. *Catal. Sci. Technol.* **2014**, *4* (9), 3129−3140.
(27) Filot, I. A.; van Santen, R. A.; Hensen, E. J. *Angew. Chem., Int. Ed.* **2014**, *53* (47), 12746−12750.
(28) Filot, I. A. W.; Shetty, S. G.; Hensen, E. J. M.; van Santen, R. A. *J. Phys. Chem. C* **2011**, *115* (29), 14204−14212.
(29) Zhang, J.; Cao, X. M.; Hu, P.; Zhong, Z.; Borgna, A.; Wu, P. *J. Phys. Chem. C* **2011**, *115* (45), 22429−22437.
(30) Liu, Z.-P.; Hu, P. *J. Am. Chem. Soc.* **2002**, *124* (39), 11568−11569.
(31) Liu, Z.-P.; Hu, P. *J. Chem. Phys.* **2001**, *114* (19), 8244−8247.
(32) Wang, J.; Liu, Z.; Zhang, R.; Wang, B. *J. Phys. Chem. C* **2014**, *118* (39), 22691−22701.
(33) Mei, D.; Rousseau, R.; Kathmann, S. M.; Glezakou, V.-A.; Engelhard, M. H.; Jiang, W.; Wang, C.; Gerber, M. A.; White, J. F.; Stevens, D. J. *J. Catal.* **2010**, *271* (2), 325−342.
(34) Chen, J.; Liu, Z.-P. *J. Am. Chem. Soc.* **2008**, *130* (25), 7929−7937.
(35) Chiu, C.-c.; Genest, A.; Rösch, N. *Top. Catal.* **2013**, *56* (11), 874−884.

DOI: 10.1021/acscatal.5b01391
ACS Catal. 2015, 5, 5453−5467

(36) Choi, Y.; Liu, P. *Catal. Today* **2011**, *165* (1), 64−70.
(37) Guo, W.; Li, M.; Lu, X.; Zhu, H.; Li, Y.; Li, S.; Zhao, L. *Dalton Trans.* **2013**, *42* (6), 2309−2318.
(38) Li, M.; Guo, W.; Jiang, R.; Zhao, L.; Shan, H. *Langmuir* **2009**, *26* (3), 1879−1888.
(39) Kozuch, S.; Shaik, S. *J. Am. Chem. Soc.* **2006**, *128* (10), 3355−3365.
(40) Kozuch, S.; Shaik, S. *J. Phys. Chem. A* **2008**, *112* (26), 6032−6041.
(41) Stegelmann, C.; Andreasen, A.; Campbell, C. T. *J. Am. Chem. Soc.* **2009**, *131* (23), 8077−8082.
(42) Stegelmann, C.; Schiødt, N. C.; Campbell, C. T.; Stoltze, P. *J. Catal.* **2004**, *221* (2), 630−649.
(43) Kresse, G.; Joubert, J. *Phys. Rev. B: Condens. Matter Mater. Phys.* **1999**, *59*, 1758.
(44) Kresse, G.; Hafner, J. *Phys. Rev. B: Condens. Matter Mater. Phys.* **1994**, *49*, 14251.
(45) Kresse, G.; Furthmüller, J. *Comput. Mater. Sci.* **1996**, *6*, 15.
(46) Perdew, J. P.; Burke, K.; Ernzerhof, M. *Phys. Rev. Lett.* **1996**, *77*, 3865.
(47) Henkelman, G.; Jónsson, H. *J. Chem. Phys.* **2000**, *113*, 9978−9985.
(48) Kittel, C. *Introduction to Solid State Physics* 8th ed.; John Wiley and Sons, Inc.: Hoboken, NJ, 2005.
(49) Jansen, A. P. J. *An Introduction to Kinetic Monte Carlo Simulations of Surface Reactions*; Springer: Berlin, Heidelberg, 2012.
(50) Filot, I. A. W.; Zijlstra, B.; Hensen, E. J. M. MKMCXX, a C++ program for constructing microkinetic models. http://www.mkmcxx.nl.
(51) Mavrikakis, M.; Bäumer, M.; Freund, H.-J.; Nørskov, J. K. *Catal. Lett.* **2002**, *81*, 153.
(52) Joos, L.; Filot, I. A. W.; Cottenier, S.; Hensen, E. J. M.; Waroquier, M.; Van Speybroeck, V.; van Santen, R. A. *J. Phys. Chem. C* **2014**, *118* (10), 5317−5327.
(53) Cheng, J.; Hu, P.; Ellis, P.; French, S.; Kelly, G.; Lok, C. M. *J. Phys. Chem. C* **2009**, *113* (20), 8858−8863.
(54) Sexton, B. A.; Somorjai, G. A. *J. Catal.* **1977**, *46* (2), 167−189.
(55) Gronchi, P.; Marengo, S.; Mazzocchia, C.; Tempesti, E.; Del Rosso, R. *React. Kinet. Catal. Lett.* **1997**, *60* (1), 79−88.
(56) Mazzocchia, C.; Tempesti, E.; Gronchi, P.; Giuffrè, L.; Zanderighi, L. *J. Catal.* **1988**, *111* (2), 345−352.
(57) Levin, M. E.; Salmeron, M.; Bell, A. T.; Somorjai, G. A. *J. Catal.* **1987**, *106* (2), 401−409.
(58) Hanaoka, T.; Arakawa, H.; Matsuzaki, T.; Sugi, Y.; Kanno, K.; Abe, Y. *Catal. Today* **2000**, *58* (4), 271−280.
(59) Van Santen, R. A.; Markvoort, A. J.; Filot, I. A. W.; Ghouri, M. M.; Hensen, E. J. M. *Phys. Chem. Chem. Phys.* **2013**, *15* (40), 17038−17063.

DOI: 10.1021/acscatal.5b01391
ACS Catal. 2015, 5, 5453−5467